Computational Materials Science 68 (2013) 320–324

Contents lists available at SciVerse ScienceDirect

Computational Materials Science

journal homepage: www.elsevier.com/locate/commatsci

A first principles investigation of the mechanical properties of *g*-ZnO: The graphene-like hexagonal zinc oxide monolayer

Qing Peng *, Chao Liang, Wei Ji, Suvranu De

Department of Mechanical, Aerospace and Nuclear Engineering, Rensselaer Polytechnic Institute, Troy, NY 12180, USA

ARTICLE INFO

Article history:
Received 5 October 2012
Accepted 16 October 2012

Keywords:
Mechanical properties
High order elastic constants
Density functional theory
2D materials
Honeycomb structure
g-ZnO

ABSTRACT

We investigate the mechanical properties, including high order elastic constants, of the graphene-like hexagonal zinc oxide monolayer (*g*-ZnO) using first-principles calculations based on density-functional theory. Compared to the graphene-like hexagonal boron nitride monolayer (*g*-BN), *g*-ZnO is much softer, with 17% in-plane stiffness and 36%, 33%, and 33% ultimate strengths in *armchair*, *zigzag*, and *biaxial* strains respectively. However, *g*-ZnO has a larger Poisson's ratio, 0.667, about three times that of *g*-BN. It was found that the *g*-ZnO also sustains much smaller strains before the rupture. We obtained the second, third, fourth, and fifth order elastic constants for a rigorous continuum description of the elastic response of *g*-ZnO. The second order elastic constants, including in-plane stiffness, are predicted to monotonically increase with pressure while the Poisson's ratio monotonically decreases with increasing pressure.

1. Introduction

With a wide bandgap (3.37 eV), a large exciton biding energy (60 meV), piezoelectricity, chemical stability, and biocompatibility, zinc oxide (ZnO) is a verstile functional material and is widely used in optics, photonics, and electronics. The applications includes light-emitting diodes, solar cells, field effect transistors, mechanical actuators, piezoelectric sensors, surface acoustic wave devices, waveguides, photocatalysts, and nanogenerators [1–3]. A hexagonal zinc oxide monolayer (*g*-ZnO) is a graphene-like 2D material, which is only monoatomically thick (Fig. 1) and chemically stable from both *ab initio* DFT calculations [4–7] and experiment [8]. The electronic and magnetic properties were extensively studied [9–16], as well as the elasticity and piezoelectricity [5,7]. The bandgap of *g*-ZnO is predicted to be 3.57–5.64 eV [7,9], larger than that in bulk. The in-plane Young's modulus was reported to be 24% of graphene [7]. The Poisson ratio is 0.71.

Two-dimentional (2D) nanomaterials are the basic "building blocks" for all other structures: buckyballs (0D) by wrapping, nanotubes (1D) by rolling, bulk (3D) by stacking [17]. However, due to the quantum confinement resulting from the reduction of the third dimention, 2D nanomaterials present very different properties from bulk. For example, the mechanical strengths are an order of magnitude larger than those in bulk. Mechanical properties are critical in designing parts or structures with *g*-ZnO regarding the practical applications. Strain engineering is a common and important approach tailoring the functional and structural properties of nanomaterials [18,9]. One can expect that the properties of *g*-ZnO will be affected by applied strain too. In addition, *g*-ZnO is vulnerable to be strained with or without intent because of its monatomic thickness. For example, there are strains because of the mismatch of lattices constants or surface corrugation with substrates [19,20]. Therefore, the knowledge of the mechanical properties of *g*-ZnO is highly desired.

Depending on the loading, the mechanical properties are divided into four strain domains: linear elastic, nonlinear elastic, plastic, and fracture. Materials in the first two strain domains are reversible, i.e., they can restore to equilibrium status after the release of the loads. On the contrary, the last two domains are nonreversible. Defects are nucleated and accumulated with the increase of the strain, until rupture. As in graphene, the nonlinear mechanical properties are prominent since it remained elastic until the intrinsic strength was reached [21,22]. Thus it is of great interest to examine the nonlinear elastic properties of *g*-ZnO, which is necessary to understand the strength and reliability of structures and devices made of *g*-ZnO.

Several previous studies have shown that 2D monolayers present a large nonlinear elastic deformation during the tensile strain up to the ultimate strength of the material, followed by a strain softening until fracture [23–26,22]. We expect that the *g*-ZnO behaves in a similar manner. Under large deformation, the strain energy density needs to be expanded as a function of strain in a Taylor series to include quadratic and higher order terms. The higher order terms account for both nonlinearity and strain

* Corresponding author. Tel.: +1 518 279 6669; fax: +1 518 276 6025.
E-mail address: pengq3@rpi.edu (Q. Peng).
URL: http://qpeng.org (Q. Peng).

0927-0256/$ - see front matter © 2012 Elsevier B.V. All rights reserved.
http://dx.doi.org/10.1016/j.commatsci.2012.10.019

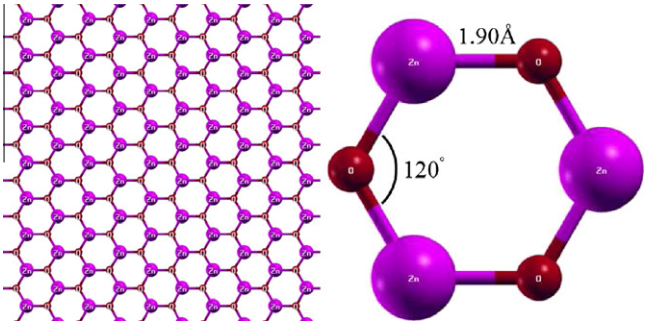

Fig. 1. Left: *g*-ZnO plane. Right: geomoetry of a conventional *g*-ZnO cell.

softening of the elastic deformation. They can also express other anharmonic properties of 2D nanostructures including phenomena such as thermal expansion and phonon–phonon interaction [21].

Due to a large bandgap, ZnO is an alternative material to the nitride semiconductors. Thus it is interesting to compare the mechanical properties of *g*-ZnO with *g*-BN, the graphene analogue of BN [27]. The goal of this paper is to study the mechanical behaviors of *g*-ZnO at large strains and find an accurate continuum description of the elastic properties from *ab initio* density functional theory calculations. The total energies of the system, forces on each atom, and stresses on the simulation boxes are directly obtained from DFT calculations. The response of *g*-ZnO under the nonlinear deformation and fracture is studied, including ultimate strength and ultimate strain. The high order elastic constants are obtained by fitting the stress–strain curves to analytical stress–strain relationships that belong to the continuum formulation [24]. We compared *g*-ZnO with the well known 2D materials such as *g*-BN, graphene, and graphyne [28]. Based on our result of the high order elastic constants, the pressure dependence properties, such as sound velocities and the second order elastic constants, including the in-plane stiffness, are predicted. Our results for the continuum formulation could also be useful in finite element modeling of the multiscale calculations for mechanical properties of *g*-ZnO at the continuum level. The remainder of the paper is organized as follows. Section 2 presents the computational details of DFT calculations. The results and analysis are in Section 3, followed by conclusions in Section 4.

2. Density functional theory calculations

We consider a conventional unit cell containing six atoms (3 Zinc atoms and 3 oxygen atoms) with periodic boundary conditions (Fig. 2). The 6-atom conventional unit cell is chosen to capture the "soft mode", which is a particular normal mode exhibiting an anomalous reduction in its characteristic frequency and leading to mechanical instability. This soft mode is a key factor in limiting the strength of monolayer materials and can only be captured in unit cells with hexagonal rings [29].

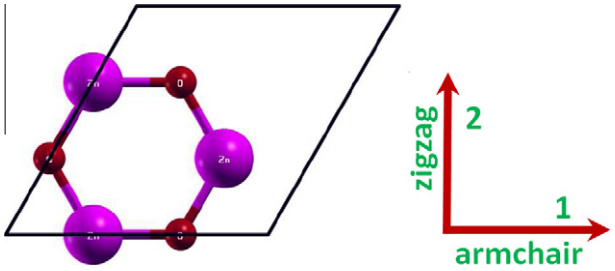

Fig. 2. Atomic structure of *g*-ZnO in the conventional unit cell (six atoms) in the undeformed reference configuration.

The total energies of the system, forces on each atom, stresses, and stress–strain relationships of *g*-ZnO under the desired deformation configurations are characterized via first-principles calculations with density-functional theory (DFT). DFT calculations were carried out with the Vienna *ab-initio* Simulation Package (VASP) [30–33] which is based on the Kohn–Sham Density Functional Theory (KS-DFT) [34,35] with the generalized gradient approximations as parameterized by Perdew, Burke, and Ernzerhof (PBE) for exchange–correlation functions [36]. The electrons explicitly included in the calculations are the $3d^{10}4s^2$ electrons for zinc atoms and $2s^22p^6$ for oxygen atoms. The core electrons are replaced by the projector augmented wave (PAW) and pseudo-potential approach [37,38]. A plane-wave cutoff of 500 eV is used in all the calculations. The calculations are performed at zero temperature.

The criterion to stop the relaxation of the electronic degrees of freedom is set by total energy change to be smaller than 0.000001 eV. The optimized atomic geometry was achieved through minimizing Hellmann–Feynman forces acting on each atom until the maximum forces on the ions were smaller than 0.001 eV/Å.

The atomic structures of all the deformed and undeformed configurations were obtained by fully relaxing a 6-atom-unit cell where all atoms were placed in one plane. The simulation invokes periodic boundary conditions for the two in-plane directions while the displacement to out-of-plane direction is forbidden.

The irreducible Brillouin Zone was sampled with a Gamma-centered $21 \times 21 \times 1$ *k*-mesh. Such a large *k*-mesh was used to reduce the numerical errors caused by the strain of the systems. The initial charge densities were taken as a superposition of atomic charge densities. There was a 15 Å thick vacuum region to reduce the inter-layer interaction to model the single layer system. To eliminate the artificial effect of the out-of-plane thickness of the simulation box on the stress, we used the second Piola–Kirchhoff stress [25] to express the 2D forces per length with units of N/m.

For a general deformation state, the number of independent components of the second, third, fourth, and fifth order elastic tensors are 21, 56, 126, and 252 respectively. However, there are only fourteen independent elastic constants that need to be explicitly considered due to the symmetries of the atomic lattice point group D_{6h} which consists of a sixfold rotational axis and six mirror planes [22].

The fourteen independent elastic constants of *g*-ZnO were determined by a least-squares fit to the stress–strain results from DFT based first-principles studies in two steps, detailed in our previous work [25]. In the first step, we used a least-squares fit of five stress–strain responses. Five relationships between stress and strain are necessary because there are five independent fifth-order elastic constants (FFOECs). We obtain the stress–strain relationships by simulating the following deformation states: uni-axial strain in the zigzag direction (*zigzag*); uni-axial strain in the armchair direction (*armchair*); and equibiaxial strain (*biaxial*). From the first step, the components of the second-order elastic constants (SOECs), the third-order elastic constants (TOECs), and the fourth-order elastic constants (FOECs) are *over*-determined (i.e, the number of linearly independent variables is *greater* than the number of constraints), and the fifth-order elastic constants (FFOECs) are *well*-determined (the number of linearly independent variables is *equal* to the number of constraints). Under such circumstances, a second step is needed: a least-square solution to these over- and well-determined linear equations.

3. Results and analysis

3.1. Atomic structure

We first optimize the equilibrium lattice constant for *g*-ZnO. The total energy as a function of lattice spacing is obtained by specifying nine lattice constants varying from 3.0 Å to 3.6 Å, with full

relaxations of all the atoms. A least-square fit of the energies versus lattice constants with a fourth-order polynomial function yields the equilibrium lattice constant as $a = 3.291$ Å. The most energetically favorable structure is set as the strain-free structure in this study and the atomic structure, as well as the conventional cell, is shown in Fig. 2. Specifically, the bond length of Zn–O bond is 1.90 Å. The Zn–O–Zn and O–Zn–O angles are 120° and all atoms are within one plane. Our results of atomic structure is in good agreement with previous DFT calculations [4–7,9–16] and experiment (1.92 Å) [8].

3.2. Strain energy

When the strains are applied, all the atoms are allowed full freedom of motion within their plane. A quasi-Newton algorithm is used to relax all atoms into equilibrium positions within the deformed unit cell that yields the minimum total energy for the imposed strain state of the super cell.

Both compression and tension are considered with Lagrangian strains ranging from −0.1 to 0.4 with an increment of 0.01 in each step for all three deformation modes. We define strain energy per atom $E_s = (E_{tot} - E_0)/n$, where E_{tot} is the total energy of the strained system, E_0 is the total energy of the strain-free system, and $n = 6$ is the number of atoms in the unit cell. This size-independent quantity is used for the comparison between different systems. Fig. 3 shows the E_s of *g*-ZnO as a function of strain in uniaxial armchair, uniaxial zigzag, and biaxial deformation. E_s is seen to be anisotropic with strain direction. E_s is nonsymmetrical for compression ($\eta < 0$) and tension ($\eta > 0$) for all three modes. This nonsymmetry indicates the anharmonicity of the *g*-ZnO structures. The harmonic region where the E_s is a quadratic function of applied strain can be taken between $-0.02 < \eta < 0.02$. The stresses, derivatives of the strain energies, are linearly increasing with the increase of the applied strains in the harmonic region. The anharmonic region is the range of strain where the linear stress–strain relationship is invalid and higher order terms are not negligible. With even larger loading of strains, the systems will undergo irreversible structural changes, and the systems are in a plastic region where they may fail. The maximum strain in the anharmonic region is the *critical* strain. The critical strain is 0.18 under armchair deformation. However, for the other two directions, the critical strains are not observed. The ultimate strains are determined as the corresponding strain of the ultimate stress, which is the maxima of the stress–strain curve, as discussed in the following section.

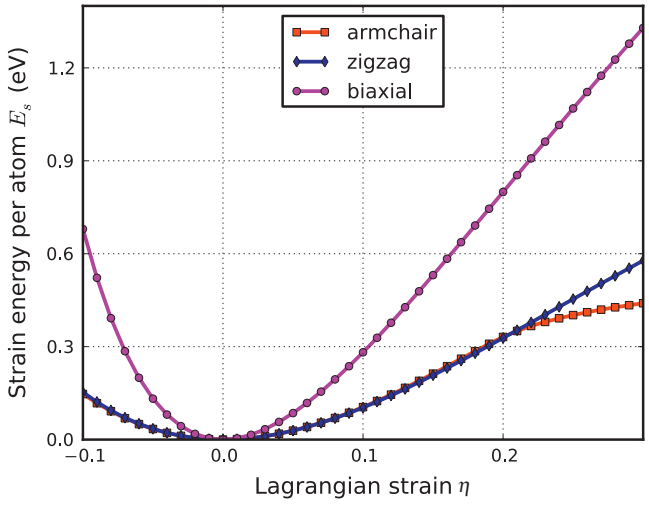

Fig. 3. Energy-strain responses for uniaxial strain in armchair and zigzag directions, and biaxial strains.

3.3. Stress–strain curves

The second *P–K* stress versus Lagrangian strain relationship for uniaxial strains along the armchair and zigzag directions, as well as biaxial strains, are shown in Fig. 4. The stresses are the derivatives

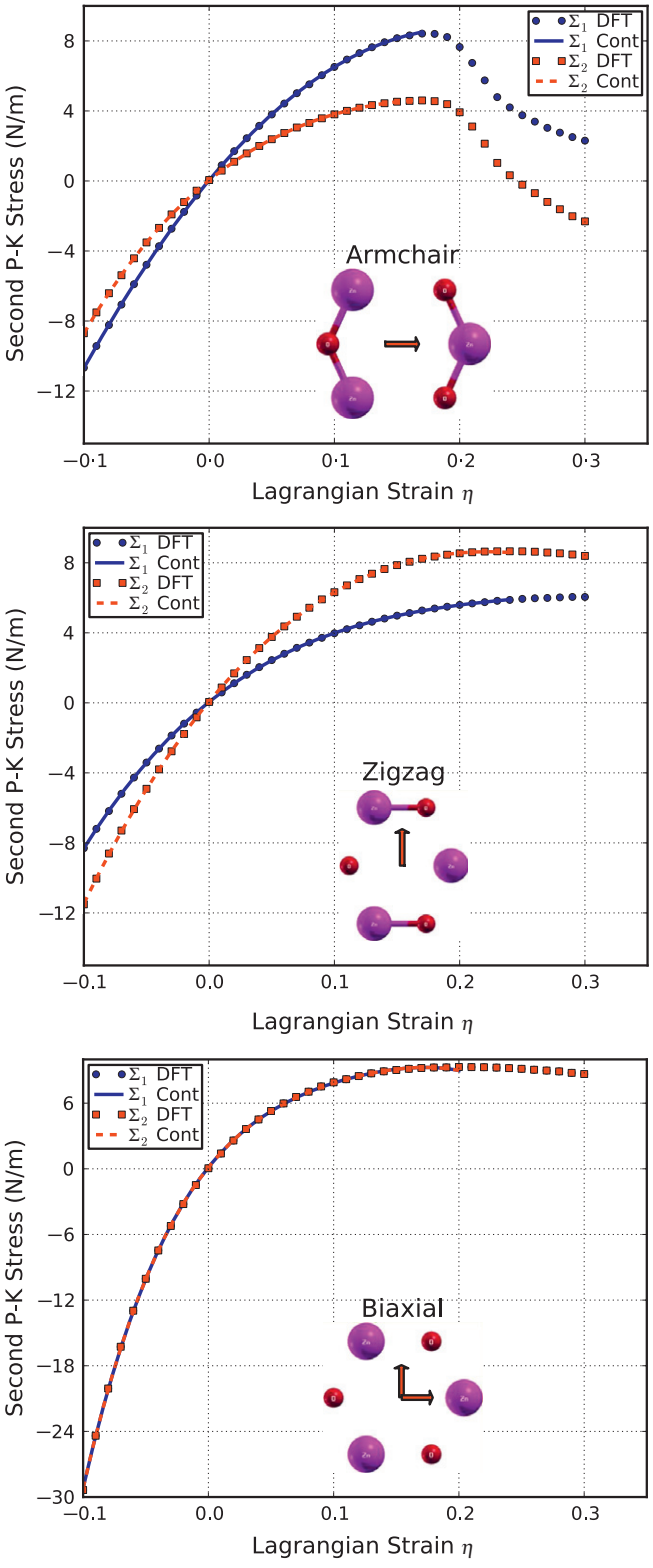

Fig. 4. Stress–strain responses of *g*-ZnO (left) and graphene (right) under the armchair, zigzag, and biaxial strain. Σ_1 (Σ_2) denotes the x (y) component of stress. "Cont" stands for the fitting of DFT calculations ("DFT") to continuum elastic theory.

Table 1
Ultimate strengths $\left(\Sigma_m^a, \Sigma_m^z, \Sigma_m^b\right)$ in units of N/m and ultimate strains $(\eta_m^a, \eta_m^z, \eta_m^b)$ under uniaxial strain (armchair and zigzag) and biaxial from DFT calculations, compared with *g*-BN, graphene, and graphyne.

	g-ZnO	*g*-BN [24]	Graphene [23]	Graphyne [26]
Σ_m^a	8.4	23.6	28.6	17.8
η_m^a	0.17	0.18	0.19	0.20
Σ_m^z	8.7	26.3	30.4	18.8
η_m^z	0.24	0.26	0.23	0.20
Σ_m^b	9.3	27.8	32.1	20.64
η_m^b	0.20	0.24	0.23	0.18

of the strain energies with respect to the strains. The ultimate strength is the maximum stress that a material can withstand while being stretched, and the corresponding strain is the ultimate strain. Under ideal conditions, the critical strain is larger than the ultimate strain. The systems of perfect *g*-ZnO under strains beyond the ultimate strains are in a metastable state, which can be easily destroyed by long wavelength perturbations and vacancy defects, as well as high temperature effects [39]. The ultimate strain is determined by the intrinsic bonding strengths and acts as a lower limit of the critical strain. Thus it has a practical meaning in consideration for its applications.

The ultimate strengths and strains corresponding to the different strain conditions are in Table 1, compared with that of *g*-BN, graphene, and graphyne. The material behaves in an asymmetric manner with respect to compressive and tensile strains. With increasing strains, the Zn–O bonds are stretched and eventually rupture. When the strain is applied in the armchair direction, the bonds of those parallel with this direction are more severely stretched than those in other directions. The ultimate strain in armchair deformation is 0.17, smaller than that of *g*-BN, graphene, and graphyne. The critical strain is 0.18 under armchair deformation, where there is a significant drop of the stresses thereafter (Fig. 4 top panel), indicating the failure of the system. However, for other two directions, the critical strains are not spotted. Under the zigzag deformation, in which the strain is applied perpendicular to the armchair, there is no bond parallel to this direction. The bonds that are at an incline to the zigzag direction with an angle of 30° are more severely stretched than those in the armchair direction. The ultimate strain in this zigzag deformation is 0.24, smaller than that of *g*-BN, while bigger than that of graphene and graphyne. At this ultimate strain, the bonds that are at an incline to the armchair direction appear to be ruptured (Fig. 4 middle panel). Under the biaxial deformation, the ultimate strain is $\eta_m^b = 0.20$, which is smaller than that of *g*-BN and graphene, but larger than graphyne. At this applied ultimate strain, all the Zn–O bonds are observed to be ruptured (Fig. 4 bottom).

It should be noted that the softening of the perfect *g*-ZnO under strains beyond the ultimate strains only occur for ideal conditions. The systems under this circumstance are in a metastable state, which can be easily destroyed by long wavelength perturbations and vacancy defects, as well as high temperature effects, and enter a plastic state [39]. Thus only the data within the ultimate strain has physical meaning and was used in determining the high order elastic constants in the following subsection.

3.4. Elastic constants

The elastic constants are critical parameters in finite element analysis models for mechanical properties of materials. Our results of these elastic constants provide an accurate continuum description of the elastic properties of *g*-ZnO from *ab initio* density functional theory calculations. They are suitable for incorporation into numerical methods such as the finite element technique.

Table 2
Nonzero independent components for the SOEC, TOEC, FOEC, and FFOEC tensor components, Poisson's ratio v and in-plane stiffness Y_s of *g*-ZnO from DFT calculations, compared with *g*-BN, graphene, and graphyne.

	g-ZnO	*g*-BN [24]	Graphene [40]	Graphyne [26]
a	3.291	2.512	2.468	6.889
Y_s	47.8	278.3	340.8	162.1
v	0.667	0.225	0.178	0.429
C_{11}	86.0	293.2	352.0	198.7
C_{12}	57.3	66.1	62.6	85.3
C_{111}	−525.4	−2513.6	−3089.7	−890.9
C_{112}	−456.3	−425.0	−453.8	−872.6
C_{222}	−452.7	−2284.2	−2928.1	−1264.2
C_{1111}	1390	16,547	21,927	−7966
C_{1112}	2284	2609	2731	4395
C_{1122}	4728	2215	3888	8662
C_{2222}	56	12,288	18,779	1154
C_{11111}	−3296	−65,265	−118,791	89,000
C_{11112}	7685	−8454	−19,173	−10,393
C_{11122}	−20,648	−28,556	−15,863	−26,725
C_{12222}	−17,926	−36,955	−27,463	−15,495
C_{22222}	1607	−10,0469	−134,752	−14,262

The second order elastic constants model the linear elastic response. The higher (>2) order elastic constants are important to characterize the nonlinear elastic response of *g*-ZnO using a continuum description. These can be obtained using a least squares fit of the DFT data and are reported in Table 2. Corresponding values for graphene are also shown.

The in-plane Young's modulus Y_s and Poison's ratio v may be obtained from the following relationships: $Y_s = \left(C_{11}^2 - C_{12}^2\right)/C_{11}$ and $v = C_{12}/C_{11}$. We have $Y_s = 47.8$ (N/m) and $v = 0.667$. The in-plane stiffness of *g*-ZnO is very small compared to *g*-BN (17%), graphene (14%), and graphyne (29%). Our obtained Poisson ratio is in good agreement with a previous DFT calculation (0.71) [7].

Knowledge of higher order elastic constants is very useful in understanding the anharmonicity. Using the higher order elastic continuum description, one can calculate the stress and deformation state under uniaxial stress, rather than uniaxial strain [22]. Explicitly, when pressure is applied, the pressure dependent second-order elastic moduli can be obtained from the high order elastic continuum description [41–43,26]. The third-order elastic constants are important in understanding the nonlinear elasticity of materials such as changes in acoustic velocities due to finite strain. As a consequence, nano devices such as nano surface acoustic wave sensors and nano waveguides could be synthesized by introducing local strain [25,26].

Stress–strain curves in the previous section show that they will soften when the strain is larger than the ultimate strain. From the view of electron bonding, this is due to the bond weakening and breaking. This softening behavior is determined by the TOECs and FFOECs in the continuum aspect. The negative values of TOECs and FFOECs ensure the softening of *g*-ZnO monolayer under large strain.

The hydrostatic terms (C_{11}, C_{22}, C_{111}, C_{222}, and so on) of *g*-ZnO monolayers are smaller than those of *g*-BN and graphene, consistent with the conclusion that the *g*-ZnO is "softer". The shear terms (C_{12}, C_{112}, C_{1122}, etc.) in general are smaller than those of *g*-BN and graphene, which contributes to its high compressibility. Compared to graphene, graphyne, and *g*-BN, one can conclude that the mechanical behavior of *g*-ZnO is similar to graphyne, and much softer than graphene and *g*-BN.

3.5. Pressure effect on the elastic moduli

With third-order elastic moduli, we can study the effect of the second-order elastic moduli on the pressure p acting in the plane

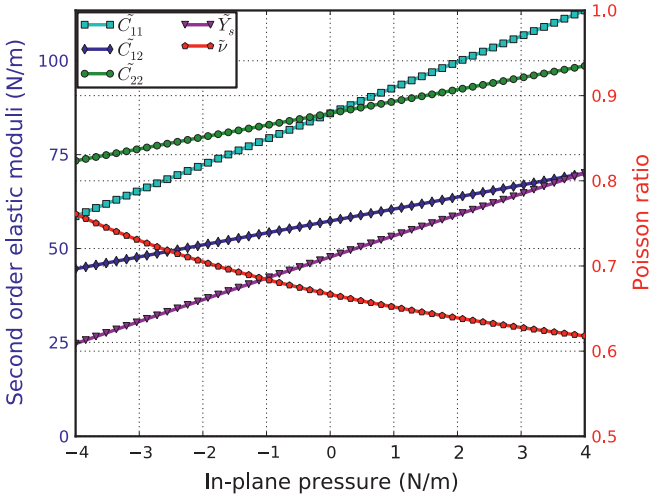

Fig. 5. Second-order elastic moduli and Poisson ratio as function of the pressure.

of *g*-ZnO. Explicitly, when pressure is applied, the pressure dependent second-order elastic moduli ($\tilde{C}_{11}$, $\tilde{C}_{12}$, $\tilde{C}_{22}$) can be obtained from C_{11}, C_{12}, C_{22}, C_{111}, C_{112}, C_{222}, Y_s, and ν as:

$$\tilde{C}_{11} = C_{11} - (C_{111} + C_{112})\frac{1-\nu}{Y_s}P \quad (1)$$

$$\tilde{C}_{22} = C_{11} - C_{222}\frac{1-\nu}{Y_s}P \quad (2)$$

$$\tilde{C}_{12} = C_{12} - C_{112}\frac{1-\nu}{Y_s}P \quad (3)$$

The second-order elastic moduli of *g*-ZnO are seen to increase linearly with the applied pressure (Fig. 5). However, Poisson's ratio decrease monotonically with the increase of pressure. $\tilde{C}_{11}$ is asymmetrical to $\tilde{C}_{22}$ unlike the zero pressure case. $\tilde{C}_{11} = \tilde{C}_{22} = C_{11}$ only occurs when the pressure is zero. This anisotropy could be the outcome of anharmonicity.

4. Conclusions

In summary, we studied the mechanical response of *g*-ZnO under various strains using DFT based first-principles calculations. It is observed that *g*-ZnO exhibits a nonlinear elastic deformation up to an ultimate strain, which is 0.17, 0.24, and 0.20 for armchair, zigzag, and biaxial directions, respectively. The deformation and failure behavior and the ultimate strength are anisotropic. It has a low in-plane stiffness (47.8 N/m) and a large Poisson ratio compared to *g*-BN and graphene. Compared to *g*-BN, *g*-ZnO has 17% in-plane stiffness, 36%, 33%, and 33% ultimate strengths in *armchair*, *zigzag*, and *biaxial* strains respectively, and a three times of Poisson's ratio. We also found that the *g*-ZnO can sustain much smaller strains before the rupture.

The nonlinear elasticity of *g*-ZnO was investigated. We found an accurate continuum description of the elastic properties of *g*-ZnO by explicitly determining the fourteen independent components of high order (up to fifth order) elastic constants from the fitting of stress–strain curves obtained from DFT calculations. This data is useful to develop a continuum description which is suitable for incorporation into a finite element analysis model for its applications at large scale. The second order elastic constants including in-plane stiffness are predicted to monotonically increase with pressure while Poisson's ratio monotonically decreases with increasing pressure.

5. Acknowledgements

The authors would like to acknowledge the generous financial support from the Defense Threat Reduction Agency (DTRA) Grant # BRBAA08-C-2-0130, the U.S. Nuclear Regulatory Commission Faculty Development Program under contract # NRC-38-08-950, and U.S. Department of Energy (DOE) Nuclear Energy University Program (NEUP) Grant # DE-NE0000325.

References

[1] Z.L. Wang, J. Phys.-Condens. Matter 16 (25) (2004) R829–R858, http://dx.doi.org/10.1088/0953-8984/16/25/R01.
[2] M. Law, L.E. Greene, J.C. Johnson, R. Saykally, P.D. Yang, Nat. Mater. 4 (6) (2005) 455–459, http://dx.doi.org/10.1038/nmat1387.
[3] Z.L. Wang, J.H. Song, Science 312 (5771) (2006) 242–246, http://dx.doi.org/10.1126/science.1124005.
[4] F. Claeyssens, C.L. Freeman, N.L. Allan, Y. Sun, M.N.R. Ashfold, J.H. Harding, J. Mater. Chem. 15 (1) (2005) 139–148, http://dx.doi.org/10.1039/b414111c.
[5] Z.C. Tu, X. Hu, Phys. Rev. B 74 (3) (2006) 035434, http://dx.doi.org/10.1103/PhysRevB.74.035434.
[6] C. Li, W. Guo, Y. Kong, H. Gao, Appl. Phys. Lett. 90 (22) (2007) 223102, http://dx.doi.org/10.1063/1.2743934.
[7] Z.C. Tu, J. Comput. Theor. Nanosci. 7 (6) (2010) 1182–1186, http://dx.doi.org/10.1166/jctn.2010.1470.
[8] C. Tusche, H.L. Meyerheim, J. Kirschner, Phys. Rev. Lett. 99 (2007) 026102, http://dx.doi.org/10.1103/PhysRevLett.99.026102.
[9] M. Topsakal, S. Cahangirov, E. Bekaroglu, S. Ciraci, Phys. Rev. B 80 (23) (2009) 235119.
[10] Y. Wang, S. Shi, Solid State Commun. 150 (31) (2010) 1473–1478.
[11] B. Kaewruksa, V. Ruangpornvisuti, J. Mol. Model. 994 (1–3) (2011) 276–282, http://dx.doi.org/10.1016/j.molstruc.2011.03.032.
[12] F.-B. Zheng, C.-W. Zhang, P.-J. Wang, H.-X. Luan, Solid State Commun. 152 (14) (2012) 1199–1202, http://dx.doi.org/10.1016/j.ssc.2012.04.066.
[13] H. Guo, Y. Zhao, N. Lu, E. Kan, X.C. Zeng, X. Wu, J. Yang, J. Phys. Chem. C 116 (20) (2012) 11336–11342, http://dx.doi.org/10.1021/jp2125069.
[14] B. Kaewruksa, V. Ruangpornvisuti, J. Mol. Model. 18 (4) (2012) 1447–1454, http://dx.doi.org/10.1007/s00894-011-1168-3.
[15] B. Kaewruksa, R. Wanbayor, V. Ruangpornvisuti, J. Mol. Model. 1012 (2012) 50–55, http://dx.doi.org/10.1016/j.molstruc.2011.12.039.
[16] F.-B. Zheng, C.-W. Zhang, P.-J. Wang, H.-X. Luan, J. Appl. Phys. 111 (4) (2012) 044329, http://dx.doi.org/10.1063/1.3688233.
[17] K.S. Novoselov, D. Jiang, F. Schedin, T.J. Booth, V.V. Khotkevich, S.V. Morozov, A.K. Geim, Proc. Natl. Acad. Sci. USA 102 (30) (2005) 10451–10453.
[18] F. Guinea, M.I. Katsnelson, A.K. Geim, Nat. Phys. 6 (1) (2010) 30–33.
[19] Y. Ma, Y. Dai, W. Wei, C. Niu, L. Yu, B. Huang, J. Phys. Chem. C 115 (41) (2011) 20237–20241, http://dx.doi.org/10.1021/jp205799y.
[20] Z.H. Aitken, R. Huang, J. Appl. Phys. 107 (12) (2010) 123531.
[21] C. Lee, X. Wei, J.W. Kysar, J. Hone, Science 321 (5887) (2008) 385.
[22] X. Wei, B. Fragneaud, C.A. Marianetti, J.W. Kysar, Phys. Rev. B 80 (20) (2009) 205407.
[23] Q. Peng, W. Ji, S. De, First-Principles study of the Effects of Mechanical Strains on the Radiation Hardness of Hexagonal Boron Nitride Monolayers, Nanoscale (2012), http://dx.doi.org/10.1039/C2NR32366D.
[24] Q. Peng, W. Ji, S. De, Comput. Mater. Sci. 56 (2012) 11.
[25] Q.Peng, A.R. Zamiri, W. Ji, S. De, Elastic Properties of Hybrid Graphene/Boron Nitride Monolayer, Acta Mechanica. 223 (2012) 2591–2596.
[26] Q. Peng, W. Ji, S. De, Mechanical Properties of Graphyne Monolayer: A First-Principles Study, Phys. Chem. Chem. Phys. 14 (2012) 13385–13391.
[27] K. Watanabe, T. Taniguchi, H. Kanda, Nat. Mater. 3 (6) (2004) 404.
[28] D. Malko, C. Neiss, F. Vines, A. Goerling, Phys. Rev. Lett. 108 (8) (2012) 086804.
[29] C.A. Marianetti, H.G. Yevick, Phys. Rev. Lett. 105 (2010) 245502.
[30] G. Kresse, J. Hafner, Phys. Rev. B 47 (1993) 558.
[31] G. Kresse, J. Hafner, Phys. Rev. B 49 (1994) 14251.
[32] G. Kresse, J. Furthuller, Phys. Rev. B 54 (1996) 11169.
[33] G. Kresse, J. Furthuller, Comput. Mater. Sci. 6 (1996) 15.
[34] P. Hohenberg, W. Kohn, Phys. Rev. 136 (3B) (1964) B864.
[35] W. Kohn, L.J. Sham, Phys. Rev. 140 (4A) (1965) A1133.
[36] J. Perdew, K. Burke, M. Ernzerhof, Phys. Rev. Lett. 77 (1996) 3865.
[37] P.E. Blöchl, Phys. Rev. B 50 (24) (1994) 17953–17979.
[38] R.O. Jones, O. Gunnarsson, Rev. Mod. Phys. 61 (3) (1989) 689–746.
[39] M. Topsakal, S. Cahangirov, S. Ciraci, Appl. Phys. Lett. 96 (9) (2010) 091912.
[40] Q. Peng, C. Liang, W. Ji, S. De, Change of nonlinear mechanical properties by hydrogenation: graphane versus graphene, submitted for publication.
[41] J.F. Nye, Physical Properties of Crystals, Oxford Science Publications, Oxford, 1995.
[42] S.Y. Davydov, Phys. Solid State 53 (3) (2011) 665.
[43] Q. Peng, S. De, Phys. E 44 (2012) 1662–1666.